Journal of Colloid and Interface Science 565 (2020) 295–304

Contents lists available at ScienceDirect

Journal of Colloid and Interface Science

journal homepage: www.elsevier.com/locate/jcis

Bimetal-organic framework derived $Cu(NiCo)_2S_4/Ni_3S_4$ electrode material with hierarchical hollow heterostructure for high performance energy storage

Wei Zhao [a,1], Guowen Yan [a,1], Yiwei Zheng [a], Bingping Liu [c], Dedong Jia [a], Taiwei Liu [a], Liang Cui [b,*], Rongkun Zheng [b], Di Wei [b], Jingquan Liu [a,b,*]

[a] College of Materials Science and Engineering, Institute for Graphene Applied Technology Innovation, Qingdao University, Qingdao 266071, Shandong, China
[b] College of Materials Science and Engineering, Linyi University, Linyi 276400, Shandong, China
[c] College of Chemistry and Pharmaceutical Sciences, Qingdao Agricultural University, Qingdao 266071, Shandong, China

GRAPHICAL ABSTRACT

Trimetallic sulfide microspheres with flower morphology prepared based on novel bimetallic MOF via sequential ion exchange processes exhibit promising energy storage properties.

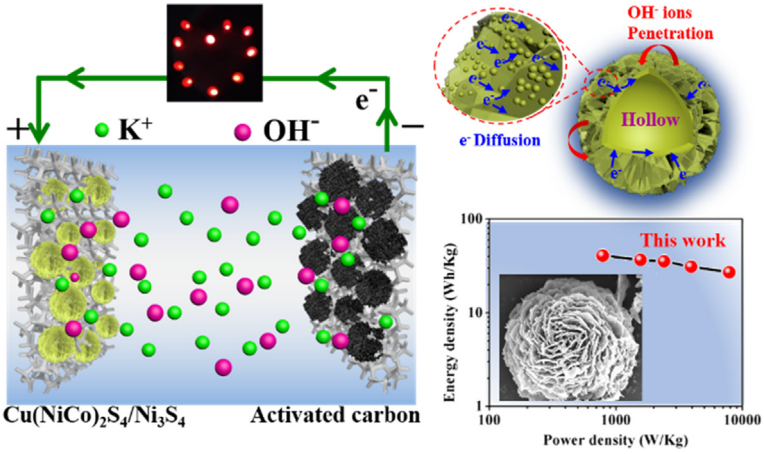

ARTICLE INFO

Article history:
Received 7 November 2019
Revised 6 January 2020
Accepted 15 January 2020
Available online 16 January 2020

Keywords:
Supercapacitor

ABSTRACT

Rational design of electrical active materials with high performance for energy storage and conversion is of great significance. Herein, $Cu(NiCo)_2S_4/Ni_3S_4$, a three-dimensional (3D) hierarchical hollow heterostructured electrode material, is designed by etching the well-defined bimetal organic framework (MOF) via sequential in-situ ion-exchange processes. This trimetallic sulfides with unique structure provide large surface area, hierarchical pore distribution and enhanced electrical conductivity, can enrich the active sites for redox reactions, facilitate electrolyte penetration and rapid charge transfer kinetics. As a result, the $Cu(NiCo)_2S_4/Ni_3S_4$ electrode exhibits a high specific capacitance of 1320 F/g at 1 A/g and excellent rate performance (only 15% of capacitance is attenuated when the current density is increased by 20

* Corresponding authors at: College of Materials Science and Engineering, Institute for Graphene Applied Technology Innovation, Qingdao University, Qingdao 266071, Shandong, China (J. Liu).
E-mail addresses: cuiliang@lyu.edu.cn (L. Cui), jliu@qdu.edu.cn (J. Liu).
[1] These authors contributed equally to this work.

https://doi.org/10.1016/j.jcis.2020.01.049

Bimetallic MOF
$Cu(NiCo)_2S_4/Ni_3S_4$/AC
Heterostructure structure
Ion-exchange

times). Furthermore, a fabricated hybrid supercapacitor of $Cu(NiCo)_2S_4/Ni_3S_4$/AC can deliver a maximum energy density of 40.8 Wh/kg, remarkable power density of 7859.2 W/kg and superior cycling stability (85% retention of capacitance after 5000 cycles), demonstrating great potential for practical applications in energy storage and conversion devices.

1. Introduction

Statistics in the World Energy Consumption report have revealed the increasing energy demand worldwide, which drives the development of energy storage and conversion devices with high performance [1,2]. Supercapacitors, due to their inherent charge storage mechanism, have higher power density but lower energy density compared to batteries, making them potential candidates for the instantaneous high power output [3]. To date, a great deal of research has been devoted to break through this bottleneck, among which reasonable selection of electrode materials, design of novel materials structure and assembly of hybrid supercapacitors (HSCs) are considered as effective methods to enhance the capacitive performance and broaden working potential [4–6].

Transition metal sulfides (TMSs) have aroused wide concern as battery-type electrode materials for HSCs due to their high electrical conductivity, rich valence states for redox reaction and a variety of stoichiometric chemistry [7]. TMSs with spinel crystal structure are usually depicted as $X_aY_{3-a}S_4$, where X and Y are two or three different metal cations with divalent and trivalent states, respectively [8]. Most often, the electronic conductivity of $X_aY_{3-a}S_4$ such as $NiCo_2S_4$ is reported to be two orders higher than their corresponding oxides and several orders higher than those of single metal sulfides, resulting in better rate performance and cycling stability [9]. Recently, $CuCo_2S_4$, another class of thiospinel with interesting electronic properties, has displayed great potential when it was utilized as energy storage electrode material. Nevertheless, $CuCo_2S_4$ is typically prepared in evacuated silica tube at temperature exceeding 500 °C, which is quite energy consuming [10]. Zhu et al. employed a hydrothermal method at 180 °C to prepare $CuCo_2S_4$ particles as battery-type electrode material, whose specific surface area (12.2 m^2/g) was relatively low, hindering the enhancement of specific capacitance due to the less exposing electrochemical active sites for redox reactions during the charge-discharge process [11]. To address the issues mentioned above, rational structure design with optimized synthetic condition deserves in depth investigation. Moreover, it can be anticipated the combination of Cu, Co, Ni and S could generate a favorable influence on the electrochemical performance enhancement, nevertheless to our best knowledge the relevant research has been rarely reported.

Three-dimensional (3D) hierarchical hollow architectures composed of two-dimensional nanosheets exhibit outstanding characteristics because of the enhanced surface area and shortened ion diffusion distance [12,13]. In view of this, metal-organic frameworks (MOF) have usually been employed as precursors or templates in many fields including catalysis [14], biomedicine [15], thermoelectricity [16], etc., due to their high surface area, porous structure and tunable morphology [17,18]. In addition, metal sulfides or oxides embedded carbon composites derived from MOF show great potentials in supercapacitors recently [19]. However, traditional MOF usually contains only single metal element, which severely limits the potential applications of the monometal-organic framework derived material [20]. Besides, particles aggregation and structure distortion of MOF tend to occur during the annealing process at high temperature, which will cause the loss of porosity and lower specific surface area, thus further failing to provide fast ion/electron transport of the derivatives and decreasing the electrochemical properties [21]. In order to optimize the structure of MOF and achieve the synergetic effects of multiple components, it is worth designing bimetal-organic framework (biMOF) with homogeneous spatial distribution of two metal elements and good morphology control via a simple fabrication method.

Herein, for the first time we have designed the 3D hierarchical hollow $Cu(NiCo)_2S_4/Ni_3S_4$ microflowers by sequential in-situ two-step ion exchange processes based on binuclear Cu_xCo_{2-x}-MOF in the presence of $Ni(NO_3)_2$ and Na_2S, during which partial cobalt ions in framework were replaced by nickel ions and the excess nickel ions deposited on the surface, then $Cu(NiCo)_2S_4/Ni_3S_4$ was formed upon the action of S^{2-}. As illustrated in Scheme 1, Cu_xCo_{2-x}-MOF was prepared originally via hydrothermal method at low temperature, the morphology of which could be regulated by adjusting the ratio of $Co(NO_3)_2$ and $Cu(NO_3)_2$. Under optimized condition, the 3D hierarchical hollow Cu_xCo_{2-x}-MOF microflowers could be obtained with Co^{2+} and Cu^{2+} radio of 1:1. Then $Ni(NO_3)_2$ was used for ion exchange, where plenty of Ni^{2+} ions were introduced into this system and biMOFs were etched simultaneously, depositing multi-metal hydroxides on the surface of these microflowers. Afterwards, these intermediates can be further converted into $Cu(NiCo)_2S_4/Ni_3S_4$ through a sequential anion exchange reaction with S^{2-}. The two-step in situ ion exchange reactions adopted in this work can realize both the structural maintaining and component control of the final products. The prepared $Cu(NiCo)_2S_4/Ni_3S_4$ delivered a high specific capacitance of 1320F/g and excellent rate performance. Moreover, the assembled HSC exhibited an outstanding energy density of 40.8 Wh/kg at a power density of 785.5 W/kg.

2. Experimental section

2.1. Preparation of CoCu-MOF precursor

Typically, $Co(NO_3)_2{\cdot}6H_2O$ and $Cu(NO_3)_2{\cdot}3H_2O$ (2 mmol totally) were dissolved in 20 mL ultrapure water followed by the quick addition of 20 mL solution containing 1.3136 g 2-methylimidazole. The resulting mixture was transferred into a Teflon-lined stainless steel autoclave with a capacity of 50 mL and the reaction was kept at 70 °C for 8 h. After naturally cooling down to room temperature (RT), the product was collected by centrifugation, washed with water and dried in vacuum at 60 °C overnight. Different molar ratios of $Co(NO_3)_2{\cdot}6H_2O$ to $Cu(NO_3)_2{\cdot}3H_2O$ (1.33:0.67, 1:1 and 0.67:1.33) were applied and the as-synthesized products were designated as $Co_{1.33}Cu_{0.67}$-MOF, Co_1Cu_1-MOF and $Co_{0.67}Cu_{1.33}$-MOF, respectively. In addition, the Co-MOF and Cu-MOF were synthesized via a same method.

2.2. Preparation of CuNiCo-OH intermediates and $Cu(NiCo)_2S_4/Ni_3S_4$

Firstly, the prepared MOFs were dispersed in 40 mL ethanol containing 0.3 g $Ni(NO_3)_2{\cdot}6H_2O$ at 50 °C for 10 min under magnetic stirring. The product (denoted as CuNiCo-OH) was collected via centrifugation and freezing dried. Next, 0.67 g $Na_2S{\cdot}9H_2O$ was dissolved in 40 mL ultrapure water followed by the addition of 64 mg CuNiCo-OH. After a quick stirring for 15 min, the mixture was

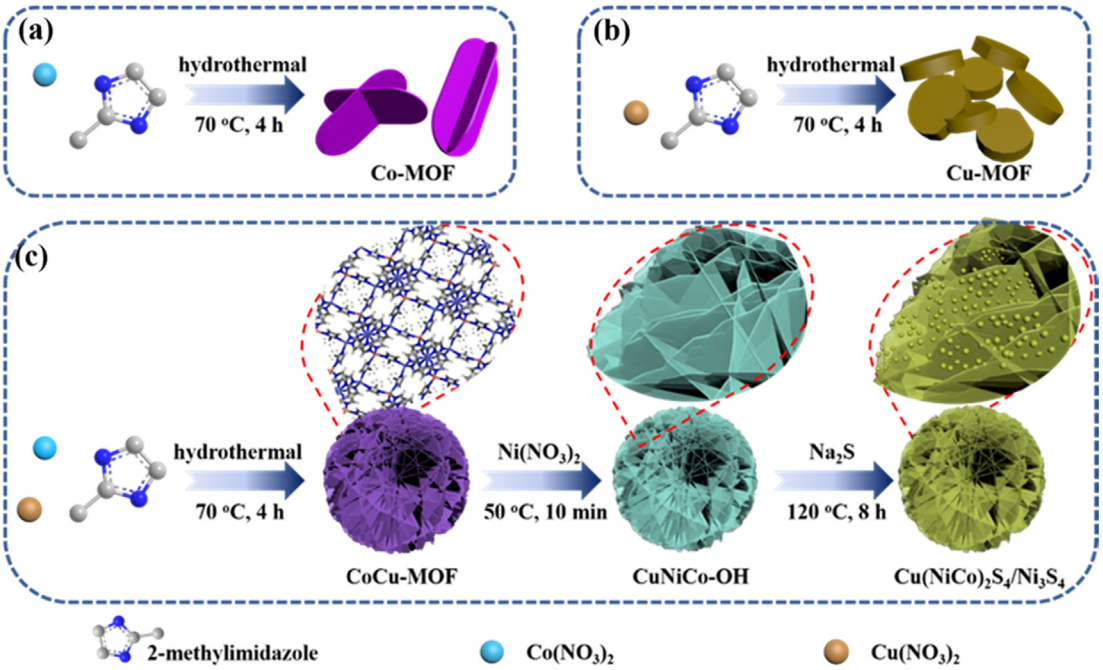

Scheme 1. (a) Schematic diagrams to illustrate the synthesis of Co-MOF (a) and Cu-MOF (b); (c) the stepwise fabrication of Cu_xCo_{2-x}-MOF and the 3D hierarchical hollow Cu $(NiCo)_2S_4/Ni_3S_4$ microflowers by sequential in-situ ion exchange reactions using $Ni(NO_3)_2$ and Na_2S respectively.

transferred into a 50 mL Taflon-lined stainless steel autoclave and heated at 120 °C for 8 h. After cooling down to RT, the obtained precipitate was separated by centrifugation and washed several times using ultrapure water to remove the impurities, followed by freeze drying to obtain the expected product.

2.3. Material and characterizations

All chemical reagents were analytical grade and used without further purification. $Cu(NO_3)_2{\cdot}3H_2O$, $Co(NO_3)_2{\cdot}6H_2O$, $Ni(NO_3)_2{\cdot}6H_2O$, $Na_2S{\cdot}9H_2O$, KOH and ethanol were provided by Sinopharm Chemical Reagent Co. Ltd. 2-Methylimidazole and PVDF was purchased from Macklin Reagent Co. Ltd (Shanghai). The morphological and structural identification of as-prepared samples were performed by field-emission scanning electron microscopy (FE-SEM, FEI Quanta200F), X-ray diffraction (XRD, D8-Advance, Bruker) and X-ray photoelectron spectroscopy (XPS, Kratos AXIS Ultra DLD spectrometer). In order to evaluate the surface area of the synthesized materials, nitrogen adsorption-desorption isotherms were obtained on a Micromeritics ASAP 2020 at 77 K and the specific surface areas were calculated via BET method.

The electrochemical performance was measured by an electrochemical station (CHI 660D). The positive electrodes were prepared by uniformly dispersing the prepared active material, acetylene black and PVDF with a mass ratio of 8:1:1 in *N*-methylpyrolidone to afford a slurry, which was loaded onto Ni foam. The positive electrode was used as working electrode, Pt as counter electrode, Hg/HgO as reference electrode and 6 M KOH as electrolyte in a three-electrode system. The electrochemical behaviors were investigated by cyclic voltammetry (CV, scan rates ranging from 5 to 50 mV/s), galvanostatic charge/discharge (GCD, current densities increasing from 1 to 20 A/g) and electrochemical impedance spectrometry (EIS, frequency varying from 100 kHz to 0.01 Hz). The specific capacitances (C_m) of prepared electrode materials were calculated by GCD according to the following equations [22]:

$$C_m = \frac{I\Delta t}{m\Delta V} \quad (1)$$

where C_m is specific mass capacitances (F/g), I means discharge current (A), Δt denotes discharging time (s), m represents the mass of active materials and ΔV refers to the operating potential window.

For assembling the hybrid supercapacitor, $Cu(NiCo)_2S_4/Ni_3S_4$ electrode was utilized as positive electrode and active carbon as negative electrode and PVA/KOH as solid state electrolyte as well as separator. The energy density (E, Wh/Kg) and power density (W/Kg) were calculated using the following equations [23]:

$$E = \frac{C(\Delta V)^2}{7.1} \quad (2)$$

$$P = \frac{3600E}{\Delta t} \quad (3)$$

where C (F/g) refers to the specific capacitance, ΔV (V) is the potential window, Δt (s) means the discharge time measured in two-electrode system with 6 M KOH as electrolyte.

3. Results and discussion

3.1. Material fabrication and characterizations

The bimetalic MOFs were prepared by a hydrothermal reaction of the mixture containing $Co(NO_3)_2{\cdot}6H_2O$, $Cu(NO_3)_2{\cdot}3H_2O$ and 2-methylimidazole at 70 °C first as shown in Scheme 1. A series of Cu_xCo_{2-x}-MOF hybrids have been prepared and the morphologies of the synthesized MOF precursors were monitored by field-emission scanning electron microscopy (FESEM). The SEM images of pure Co-MOF (Fig. S1) revealed the intersected layer structure with smooth surface, while the pure Cu-MOF exhibited independent dots with average size about 145 nm as shown in Fig. S2. The corresponding elemental mapping images indicated the uniform distribution of C, N, Co or C, N, Cu in Co-MOF or Cu-MOF, where C and N elements should come from the organic ligand 2-methylimidazole. The obtained $Co_{1.33}Cu_{0.67}$-MOF exhibited an intersected layer structure which is similar to Co-MOF as displayed in Fig. 1a–c, but its surface was dotted with a lot of nanoflowers.

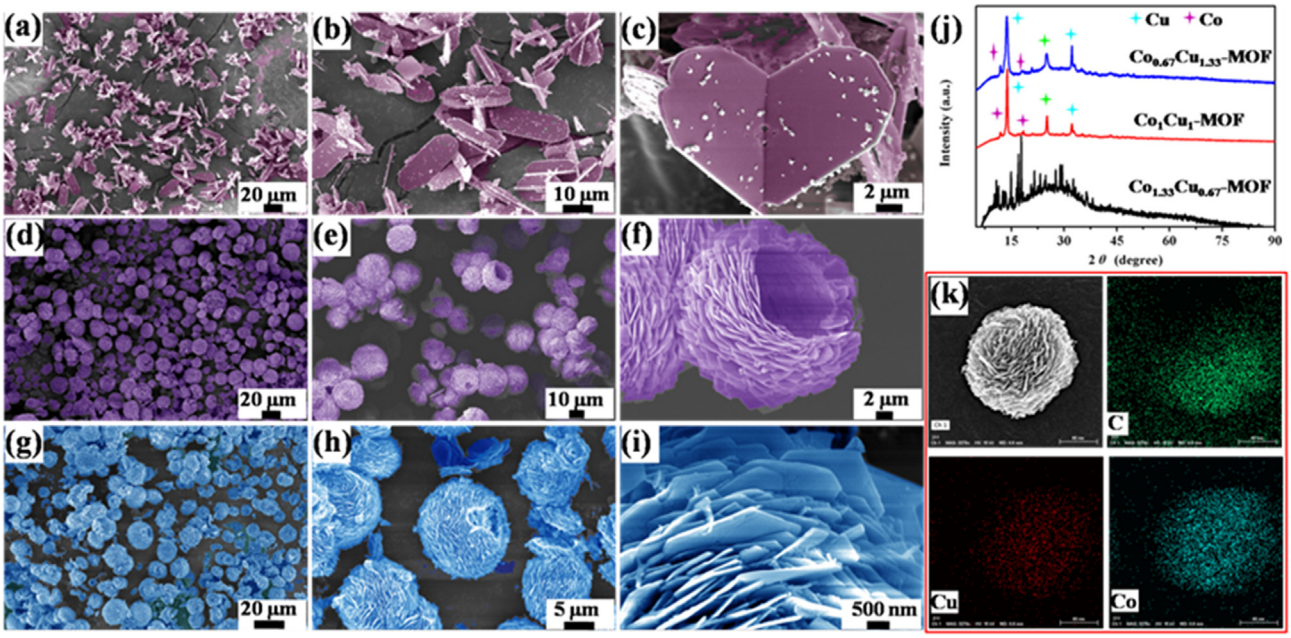

Fig. 1. (a–c) SEM images of $Co_{1.33}Cu_{0.67}$-MOF with different magnifications; (d–f) SEM images of Co_1Cu_1-MOF with different magnifications; (g–i) SEM images of $Co_{0.67}Cu_{1.33}$-MOF with different magnifications; (j) XRD patterns of the synthesized bimetallic MOFs and (k) SEM image and elemental mapping images of Co_1Cu_1-MOF.

Interestingly, a dimensional transformation occurred due to the spontaneous assembly of layers into microflowers with the increase of $Cu(NO_3)_2{\cdot}3H_2O$ input. As can be seen in Fig. 1d-e, the synthesized Co_1Cu_1-MOF possesses flower-like architecture with smaller size compared to $Co_{1.33}Cu_{0.67}$-MOF. From the highly magnified image, it can be seen that the microflowers were consisted of plenty nanosheets, which assembled into a hollow structure (Fig. 1f). These fantastic 3D flower-shaped bimetallic MOFs with hollow structure are considered to be promising template for supercapacitor application due to the high specific surface area and multiple metal ion precursors. The elemental mapping images of Co_1Cu_1-MOF are displayed in Fig. 1k, confirming the homogeneous distribution of Cu and Co elements. When the molecular ratio of Cu:Co increased to 2:1, the obtained product $Co_{0.67}Cu_{1.33}$-MOF showed almost the same 3D flower-like morphology with hollow structure as displayed in Fig. 1g–i.

To better evidence the successful synthesis of the bimetallic MOFs, XRD measurement was also carried out to analyze the crystal structure. XRD pattern of pure Co-MOF indicated a layered phase which is free from any impurities [24]. Apparent diffraction peaks at 14.4°, 29.6°, 32.9° and 34° could be observed in the XRD pattern of pure Cu-MOF (Fig. S3a). As shown in Fig. 1j, the $Co_{1.33}$-$Cu_{0.67}$-MOF exhibited the similar XRD pattern to that of Co-MOF while Co_1Cu_1-MOF and $Co_{0.67}Cu_{1.33}$-MOF displayed apparent diffraction peaks at 11.8°, 14.4°, 25° and 32°, which were similar to those observed with the pure Cu-MOF. Nevertheless, the emerge of new peak at 25° indicated that the Co_1Cu_1-MOF and $Co_{0.67}Cu_{1.33}$-MOF were not the simple mixtures of Co-MOF and Cu-MOF, but a new MOF with new crystal structure due to the synergistic effects of Co^{2+} and Cu^{2+}. Intuitively, the obvious color differences could be observed from macro photos of Co-MOF (light purple), Cu-MOF (russet) and Co_1Cu_1-MOF (deep purple) as shown in Fig. S3b. Figure S3b also presents the FTIR spectrum of the obtained MOF, where the strong absorption peak at 424 cm^{-1} could be assigned to the metal-N stretching and the broad peak at around 3500 cm^{-1} should result from the absorbed water [25]. The peaks in the range of 1100–1400 cm^{-1} can be attributed to the stretching mode of C—N in 2-methylimidazole while the absorption band at 987 cm^{-1} could contribute to the bending vibration of C—N [26]. Besides, the characteristic peak of —CH_2(υ_{as}) at 2925 cm^{-1} was also observed. The above results indicate the successful synthesis of MOF templates with different components. An hydrolysis-controlled ion exchange method was employed to prepare CoCuNi-OH intermediate through the reaction of Co_1Cu_1-MOF with $Ni(NO_3)_2$. Fig. 2a-b displays the SEM images of resultant product, from which it can be seen that the overall morphology was maintained well. From the enlarged SEM image as shown in Fig. 2c, we can see the layers become rougher with the thickness between 120 and 150 nm. Corresponding element mapping images revealed the existence and uniform distribution of large amounts of Cu, Co, Ni and O, demonstrating the successful transformation to trimetallic material. The full transformation of bimetallic MOF was also confirmed by the disappearance of bimetallic MOF diffraction peaks and the emerging peaks of multiple metal hydroxides (abbreviated as CuNiCo-OH) as shown in Fig. S4. The conversion mechanism can be illustrated by the following chemical equation:[27]

$$Ni^{2+} + H_2O \rightarrow Ni(OH)_2 + 2H^+ \quad (4)$$

It can be seen from the chemical reaction above that H^+ will be generated which could etch the organic fragments, leading to the growth of metal hydroxides. Subsequently, an anion exchange reaction was carried out between CuNiCo-OH and S^{2-} under hydrothermal condition in Na_2S solution. The XRD pattern of prepared product, displayed in Fig. 3a, matches well with spinel $Cu(NiCo)_2S_4/Ni_3S_4$ (JCPDS card: No.29-0540 and 47-1739). The morphology of the obtained $Cu(NiCo)_2S_4/Ni_3S_4$ completely inherited the microflower shape of the initial synthesized bimetallic MOF template as shown in Fig. 2e-f. As observed from the enlarged SEM image in Fig. 2g, these petal-sheets composed of numerous nanoparticles cross-connected with each other, forming abundant space among neighboring structures, which could greatly provide the large specific surface area and 3D stable channels for fast electrolyte ion/electron transport. Fig. 2h indicates uniform distribution of the Cu, Co, Ni and S elements in the $Cu(NiCo)_2S_4/Ni_3S_4$ microsphere. It is well known that the in-situ ion exchange/etching method could maximize the inheritance of original morphology and structure. Furthermore, by ions exchange, mesoporous pores

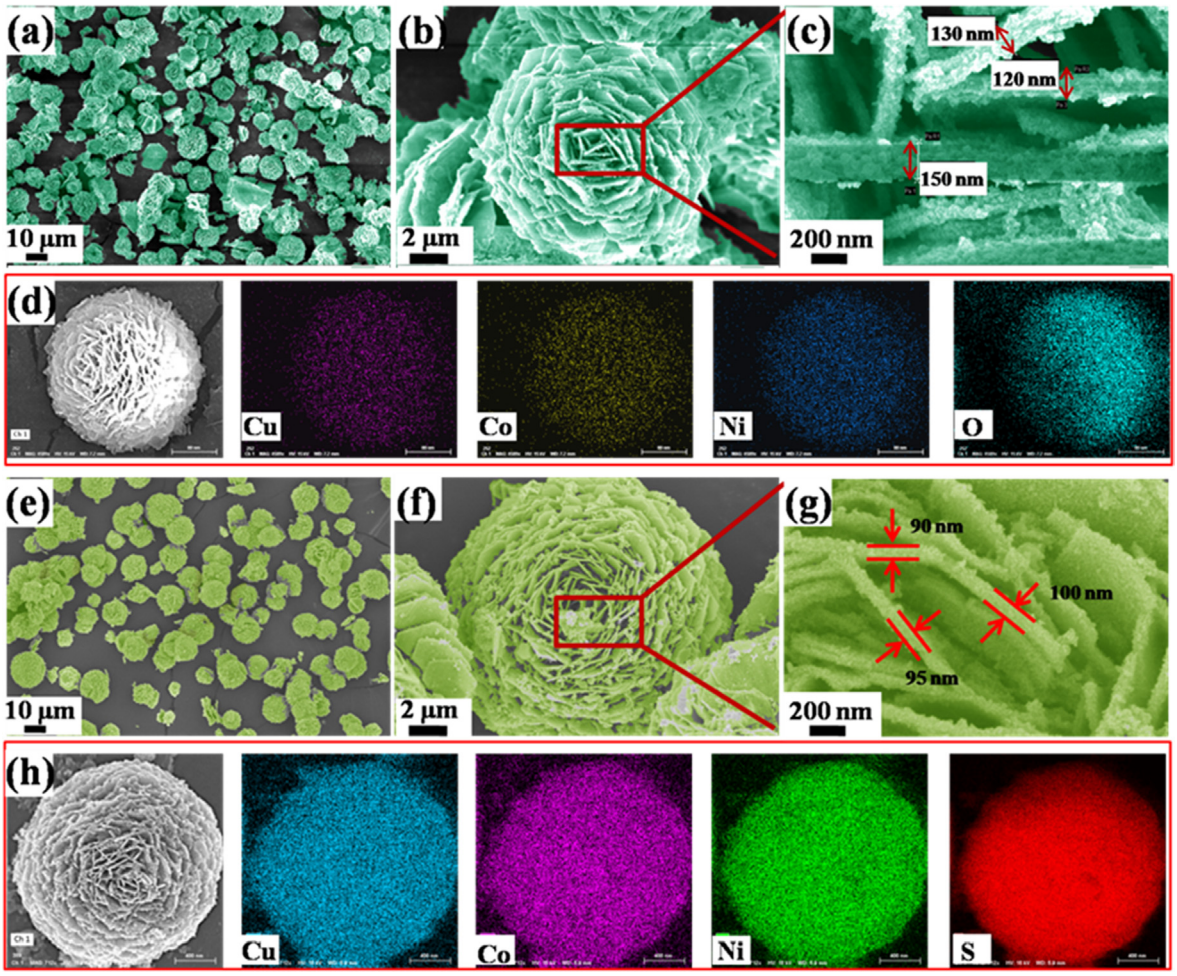

Fig. 2. (a–c) SEM images of CoCuNi-OH and (d) the corresponding elemental mapping; (e–g) SEM images of $Cu(NiCo)_2S_4/Ni_3S_4$ and (h) the corresponding elemental mapping images.

can be formed on the basis of microporous pores, which facilitates the diffusion of ions, playing an significant role in improving electrochemical performance [28]. For the insight into the prepared 3D flower-like trimetal hydroxide CuNiCo-OH and sulfide $Cu(NiCo)_2S_4/Ni_3S_4$, their N_2 adsorption–desorption isotherms and pore size distribution were measured. As shown in Fig. S5 the typical Langmuir IV type isotherms with a distinct hysteresis loop in a range of 0.6–1.0P/P_0 can be observed in Fig. S5a, demonstrating the presence of mesoporous structure. The BET surface areas of CuNiCo-OH and $Cu(NiCo)_2S_4/Ni_3S_4$ were calculated to be 52.6 m^2/g and 90.3 m^2/g, respectively. The corresponding pore size distribution in Fig. S5b calculated via the Barrett–Joyner–Halenda (BJH) method further verified the hierarchical pore structure. The pore size distribution of $Cu(NiCo)_2S_4/Ni_3S_4$ was relatively narrow and mainly concentrated in the range of 5–10 nm, which was reported to be optimal for the diffusion of ions/electrons within electrodes [29]. To further understand the elemental composition and chemical state of the prepared material, XPS measurement was carried out and the corresponding results are presented in Fig. 3 [30]. The survey spectra (Fig. 3b) show that the prepared $Cu(NiCo)_2S_4/Ni_3S_4$ contains Cu, Ni, Co and S elements. By adopting a Gaussian fitting method, the Cu 2p emission spectrum (Fig. 3c) can be deconvolved into two characteristic spin–orbit doublets of Cu^{2+} and Cu^{+} and two satellites. The fitting peaks at 934.6 eV and 955 eV are indexed to Cu^{2+}, while the other fitting peaks at 934.2 eV and 953.7 eV are ascribed to Cu^{+} [31]. In Ni 2p spectra (Fig. 3d), two kinds of Ni species could be observed and indexed to the species containing Ni^{2+} and Ni^{3+} ions. Specifically, the fitting peaks at 855.7 and 873.8 eV are attributed to Ni^{2+}, while the other two fitting peaks at 854.2 and 871.7 eV belong to Ni^{3+} [32]. As shown in Fig. 3e, the spectra of Co 2p region have Co 2p3/2 peaks at 779.1 and 781.5 eV, and Co 2p1/2 peaks at 794.1 and 797.7 eV respectively, demonstrating the coexistence of Co^{2+} and Co^{3+} [33,34]. The S 2p spectrum provided two main peaks and one shakeup satellite, which are labeled as 2p3/2 and 2p1/2. The peak of 2p3/2 located at 161.8 eV is corresponded to metal-sulfur bonds while the 2p1/2 at 162.8 eV is assigned to sulfur ions at low coordination ordinarily related to sulfur vacancies [35]. Based on the above discussion, the near surface of the $Cu(NiCo)_2S_4/Ni_3S_4$ has a mixed composition of Cu^{2+}/Cu^{+}, Ni^{3+}/Ni^{2+} and Co^{3+}/Co^{2+}, which is favorable for the enhancement of electrochemical performance for supercapacitor through providing rich Faradic reaction sites.

To investigate the electrochemical performance of the synthesized 3D $Cu(NiCo)_2S_4/Ni_3S_4$ with hierarchical flower-like structure, CV, GCD and EIS measurements were performed in a standard three-electrode system in 6 M KOH. For comparison, the intermediate CuNiCo-OH was also evaluated as a supercapacitor electrode material and detailed information could be observed in supporting information. The CV curves at the scan rate of 5 mV/s for $Cu(NiCo)_2S_4/Ni_3S_4$ and CuNiCo-OH are exhibited in Fig. 4a. Both the electrode materials showed well-defined redox peaks where the current response of $Cu(NiCo)_2S_4/Ni_3S_4$ was significantly higher than that of CuNiCo-OH, implying the better electrical conductivity of trimetallic sulfides compared to hydroxides. The redox peaks

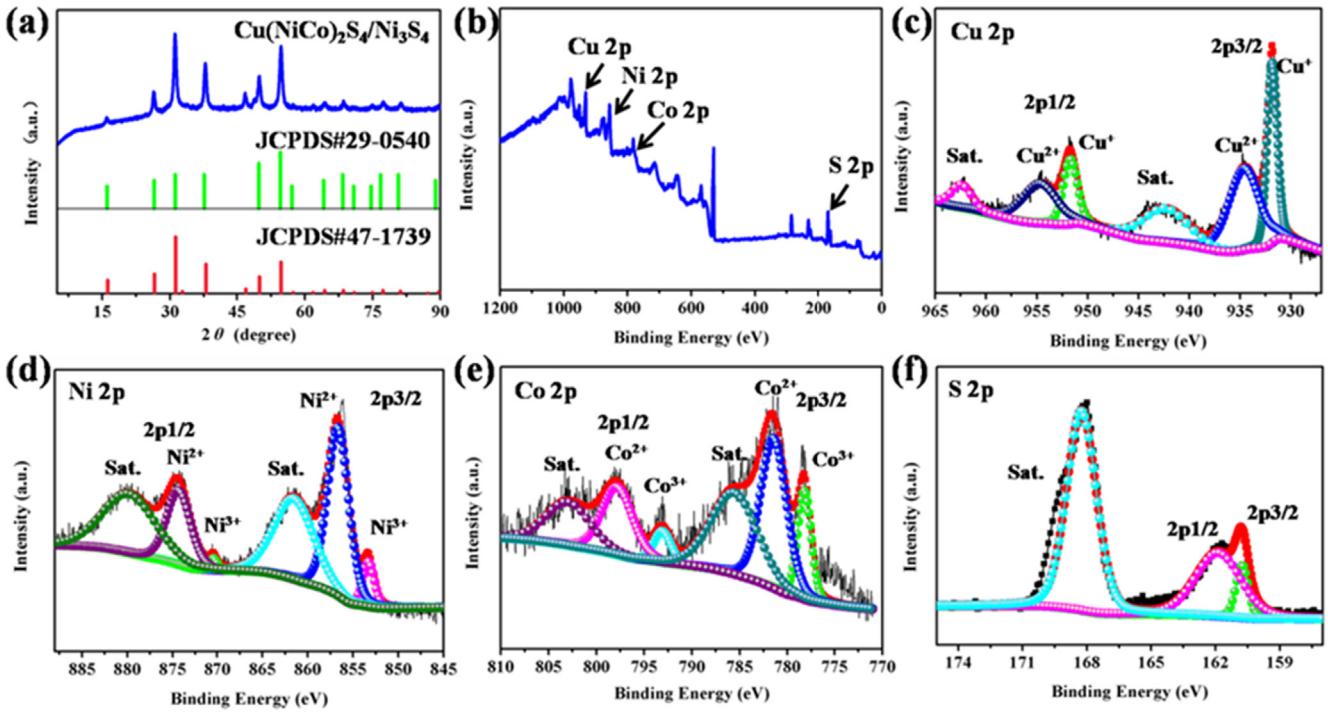

Fig. 3. (a) XRD pattern of the as-prepared $Cu(NiCo)_2S_4/Ni_3S_4$ and peak locations from the standard JCPDS card No. 29-0540 of $Cu(NiCo)_2S_4$ and No. 47-1739 of Ni_3S_4. XPS spectra of (b) survey spectrum, high resolution spectra for (c) Cu 2p, (d) Ni 2p, (e) Co 2p and (e) S 2p of $Cu(NiCo)_2S_4/Ni_3S_4$.

could be assigned to the Faradaic redox transition of M-S/M-S-OH in KOH alkaline solution, where M represents metal cations of Cu, Co, and Ni. As shown in the CV curve of $Cu(NiCo)_2S_4/Ni_3S_4$, two pairs of redox peaks could be observed, which is attributing to the transition reactions of $Cu^{2+}\leftrightarrow Cu^{+}$, $Co^{2+} \leftrightarrow Co^{3+}$ and $Ni^{2+} \leftrightarrow Ni^{3+}$. Usually, potentials for these transitions are quite close, therefore it is difficult to clarify the precise reacting mechanism during the redox process. Whereas, the separation of redox peaks for the CV curve of $Cu(NiCo)_2S_4/Ni_3S_4$ could be explained by the decrease of the concentration polarization because the further ion-exchange/etching of CuNiCo-OH with S^{2-} could increase the specific surface area and provide more active sites. Fig. 4b shows the GCD curves obtained at the current density of 1 A/g, both of which display potential plateau of redox reactions, indicating the battery-type behavior. Moreover, the discharge curve of $Cu(NiCo)_2S_4/Ni_3S_4$ possessed two potential plateaus, resulting in the much longer discharging time and higher specific capacitance than that of CuNiCo-OH, which was consistent with CV result. As shown in Fig. 4c, EIS was measured under the frequency from 100 kHz to 0.01 Hz to analyze the impedance. The equivalent circuit for the Nyquist plots of $Cu(NiCo)_2S_4/Ni_3S_4$ has also been provided in Fig. S6. In the high-frequency region, the series resistance of electrode (R_s) including the intrinsic resistance of the prepared electrode material M-S or M-OH, KOH electrolyte and contact impedance at the interface of active material and Ni foam current collector, could be determined by the real axis intercept of EIS Nyquist plot [36,37]. The R_s values were 0.65 and 1.8 O for $Cu(NiCo)_2S_4/Ni_3S_4$ and CuNiCo-OH, respectively. The semicircle in high-frequency region was used to estimate the charge transfer impedance (R_{ct}) at the interface between electrode and electrolyte. It can be clearly seen the semicircle of $Cu(NiCo)_2S_4/Ni_3S_4$ was smaller than that of CuNiCo-OH, revealing the faster charge transfer to allow the fast redox reactions. In low-frequency region, the line slope could reflect the diffusion impedance of electrolyte (R_w) and the steeper line signified the lower diffusion impedance [38–40]. Therefore, it can be confirmed that the narrow pore distribution centered at 5–10 nm of $Cu(NiCo)_2S_4/Ni_3S_4$ after sequential ion-exchange/etching reaction was actually conducive to fast electrolyte diffusion as mentioned above. In general, the low impedance of $Cu(NiCo)_2S_4/Ni_3S_4$ confirmed by R_s, R_{ct} and R_w makes it a highly conductive material, leading to faster ion/charge transfer and thereby improved specific capacitance and rate performance.

CV curves of $Cu(NiCo)_2S_4/Ni_3S_4$ obtained at the scan rate ranging from 5 to 30 mV/s are presented in Fig. S7a, from which two pairs of redox peaks could be observed, indicating the rich reversible Faradaic redox reaction due to the $Cu(NiCo)_2S_4/Ni_3S_4$ heterostructure that can provide more reactive sites. With the increasing scan rate, the adjacent redox peaks gradually merged due to the quite close potentials of these reversible processes, a phenomenon that is very common [41]. Besides, the oxidation peaks shifted to higher potential whereas the reduction peaks shifted to lower one with the increasing scan rate, which could be related to the augmentation of internal diffusion resistance, which could hinder the ion diffusion to satisfy the electronic neutralization during the fast faradic process [42]. The redox peaks in CV curve of $Cu(NiCo)_2S_4/Ni_3S_4$ could still be seen at the high scan rate of 30 mV/s, demonstrating the fast kinetics for faradic reactions and the capacity for rapid energy storage.

Nevertheless, for CuNiCo-OH system, its CV curves exhibited severe deformation even at the scan rate of 15 mV/s as shown in Fig. S8a. Fig. S7b revealed the GCD curves of $Cu(NiCo)_2S_4/Ni_3S_4$ obtained at different current densities ranging from 1 to 20 A/g. The symmetrical GCD curves without obvious iR-drop (the sudden drop in voltage at the beginning of discharge) indicated the high coulombic efficiency. According to the discharging time, the specific capacitance of $Cu(NiCo)_2S_4/Ni_3S_4$ was calculated and displayed in Fig. 4d. The specific capacitances of 1320, 1264, 1230, 1190, 1100 and 1000 F/g were achieved corresponding at the current density of 1, 2, 3, 5, 10 and 20 A/g, revealing the excellent rate capability of 75.7%. As a contrast, the specific capacitance of CuNiCo-OH was also calculated based on its GCD curves as shown in Fig. S8b. Obviously, its specific capacities of 670, 629, 600, 551,

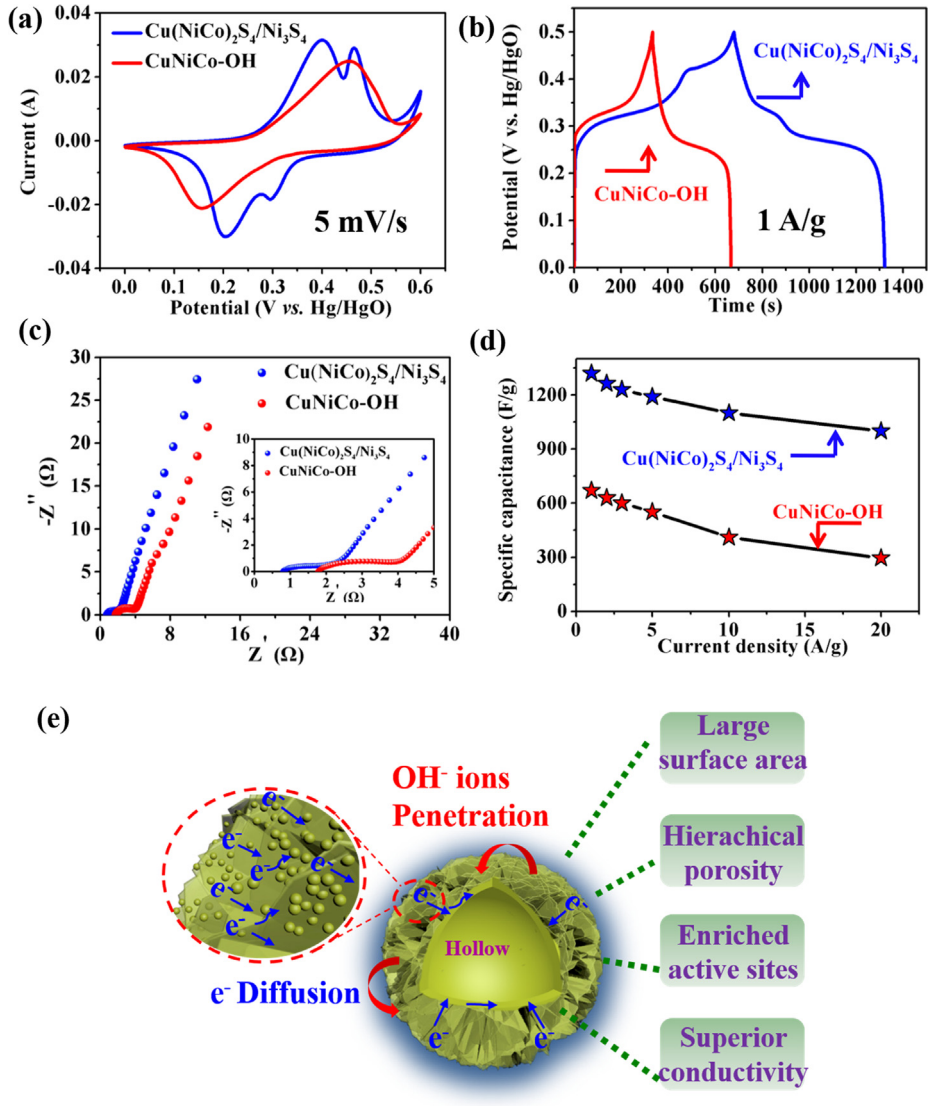

Fig. 4. Electrochemical performance measured by a three-electrode system: (a) CV curves at scan rate of 5 mV/s, (b) GCD at current density of 1 A/g and (c) EIS of $Cu(NiCo)_2S_4/Ni_3S_4$ and CuNiCo-OH. (d) Specific capacitances of $Cu(NiCo)_2S_4/Ni_3S_4$ and CuNiCo-OH as a function of current density. (e) Schematic illustration for $Cu(NiCo)_2S_4/Ni_3S_4$ electrode designs and charge storage mechanism.

410 and 296F/g at the same current densities were much lower than those of $Cu(NiCo)_2S_4/Ni_3S_4$. Furthermore, the capacitance retention was only 46%, implying the inferior rate performance.

The long-term cycling stability of $Cu(NiCo)_2S_4/Ni_3S_4$ was evaluated via GCD measurement at a high current density of 30 A/g. It can be observed from Fig. S7c that 75% of initial capacitance has been reserved after 5000 GCD cycles. The inset in Fig. S7c represents the corresponding SEM images of $Cu(NiCo)_2S_4/Ni_3S_4$ before and after the cycling test. The slight decay of capacitance could be attributed to the slight structural collapse of the $Cu(NiCo)_2S_4/Ni_3S_4$ caused by the transformation of sulfides to hydroxides during the repeated cycling process [43]. The outstanding electrochemical performance could be attributed to the following aspects as illustrated in Fig. 4e. Essentially, the 3D flower-like hollow morphology consisted of tightly stacked nanopetals will provide large surface area and hierarchical porous structure, which could expose large amounts of active sites for redox reaction to realize the maximizing utilization of electroactive materials and afford a stable structure during repeated charge/discharge process. Specifically, the abundant space between neighboring nanopetals could facilitate the electrolyte penetration and buffer the resulting strain generated from rapid intercalate/de-intercalate of OH^- ions. Moreover, the incorporation of nickel cobalt copper sulfides could lead to the enhanced conductivity and emerging of new active sites for enriched Faradic redox reactions. That is the reason why $Cu(NiCo)_2S_4/Ni_3S_4$ could deliver enhanced specific capacitance, excellent rate performance and stable cycling performance.

To further investigate the potential practical application of the synthesized $Cu(NiCo)_2S_4/Ni_3S_4$ electrode material, a two-electrode system was assembled utilizing $Cu(NiCo)_2S_4/Ni_3S_4$ as positive electrode and activated carbon (AC) as negative electrode as illustrated in Fig. 5a. It is well known the relatively low energy density has been the bottleneck that hinders the practical application of supercapacitors. In addition to explore efficient electrode material to improve the specific capacitance, assembling asymmetric or hybrid supercapacitors to broaden voltage windows could also be another promising way to enhance the energy densities of supercapacitors. Activated carbon as pervasively used negative electrode material possesses stable double layer capacitor behavior. The basic electrochemical performance of AC electrode has been studied in a three-electrode system with 6 M KOH as electrolyte before evaluating the performance of assembled HSC. The

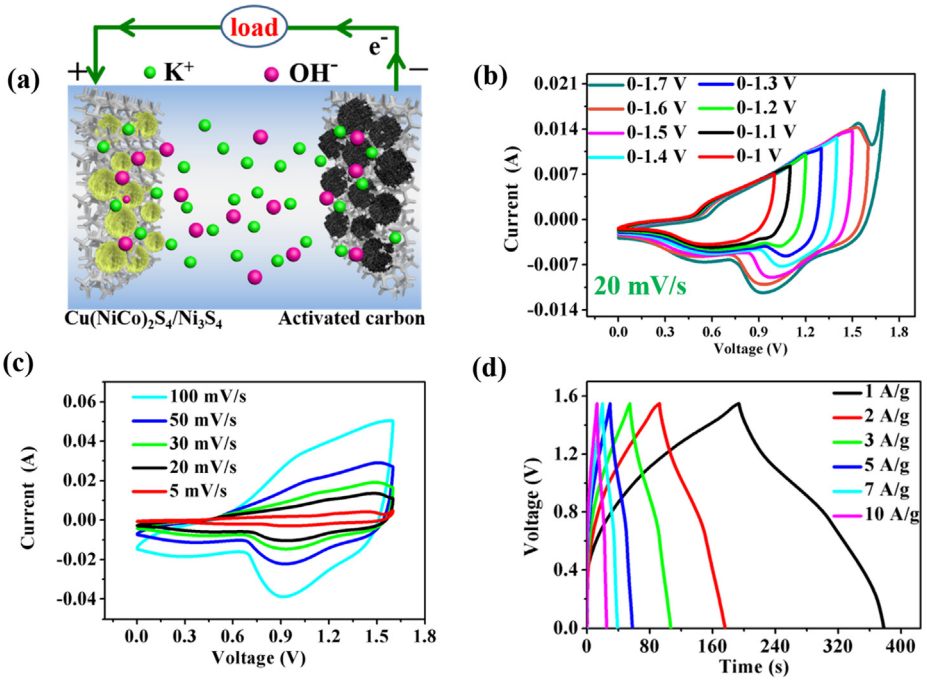

Fig. 5. Electrochemical performance of the assembled hybrid supercapacitor device: (a) The schematic illustration for the design and charge storage mechanism of Cu$(NiCo)_2S_4/Ni_3S_4$/AC HSC. (b) CV curves of the fabricated HSC operated at different voltage windows under the scan rate of 20 mV/s. (c-d) CV and GCD curves of the fabricated HSC collected at various scan rates from 5 to 100 mV/s and different current densities of 1 to 10 A/g.

CV and GCD curves are displayed in Fig. S9. The rectangle-like CV curves and symmetric triangle-like GCD curves indicated the double-layer capacitance behavior was controlled by fast ions diffusion/adsorption process, based on which the specific capacitance of AC was calculated to be as high as 198 F/g at the current density of 1 A/g. In accordance with the principle of charge conservation, $q^+ = q^-$, the mass ratio of Cu$(NiCo)_2S_4/Ni_3S_4$ and AC should be controlled at 0.25 for assembling the supercapacitor device.

As displayed in Fig. S10, the working potential windows of Cu$(NiCo)_2S_4/Ni_3S_4$ and AC were located at 0–0.6 V and −1 to 0 V, respectively. After integration of the two electrodes, CV curves measured at different potential window were recorded as shown in Fig. 5b, from which we can see the assembled HSC could deliver a maximum stable operating voltage of up to 1.6 V, whereas slight polarization occurred when the voltage range was extended to 1.7 V. Fig. 5c shows the CV curves of Cu$(NiCo)_2S_4/Ni_3S_4$/AC HSC operating at different scan rates of 5, 20, 30, 50, 100 mV/s, which contained an approximately rectangular region between 0 and 0.7 V and redox peaks at 0.7–1.6 V, revealing the capacitor behavior controlled by the integration of double-layer contribution generated from AC and battery-type contribution from Cu$(NiCo)_2S_4/Ni_3S_4$. The CV curves did not deform even at the high scan rate of 100 mV/s, which verified the excellent rate performance and reaction kinetics of the fabricated HSC. GCD measurement was further

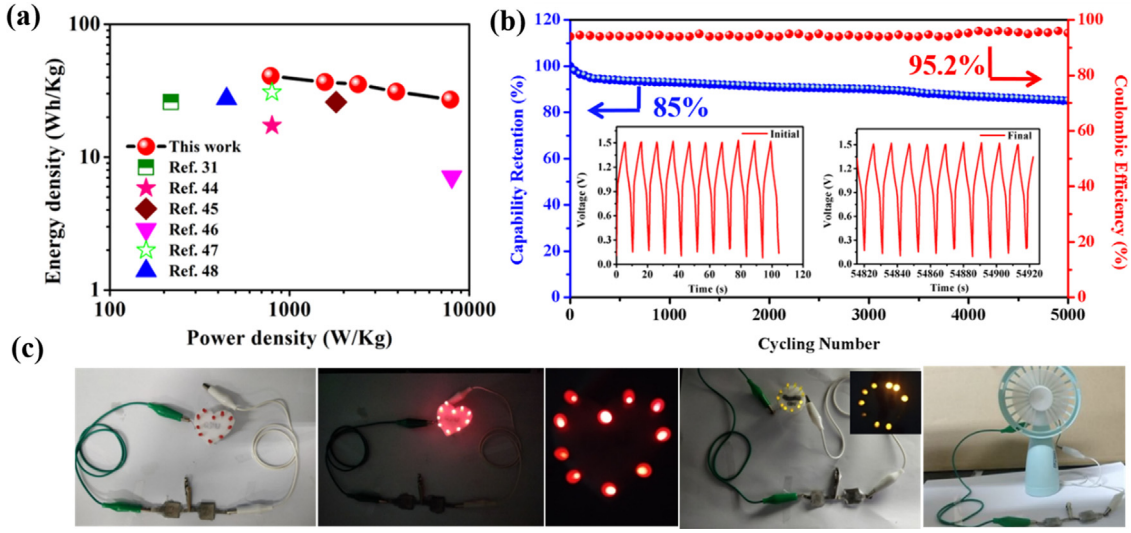

Fig. 6. (a) Ragone plot related to energy densities and power densities of Cu$(NiCo)_2S_4/Ni_3S_4$/AC HSC and comparison with other reported nickel cobalt or copper based HSC devices. (b) The long-term stability of Cu$(NiCo)_2S_4/Ni_3S_4$/AC HSC for 5000 cyclic tests and the inset shows the initial and final 10 cycles. (c) Two Cu$(NiCo)_2S_4/Ni_3S_4$/AC HSCs connected in series to light the red and yellow LED and drive the fan motor. (For interpretation of the references to color in this figure legend, the reader is referred to the web version of this article.)

carried out at the current densities of 1, 2, 3, 5, 10 and 20 A/g. As shown in Fig. 5d the symmetric charge-discharge curve indicated the excellent reversibility for redox reactions and coulombic efficiency of HSC. Moreover, the calculated specific capacitances of $Cu(NiCo)_2S_4/Ni_3S_4$/AC HSC at current densities ranging from 1 to 20 A/g are shown in Fig. S11. The assembled HSC could deliver a specific capacitance of 120.6F/g at 1 A/g and maintained 80 F/g at the high current density of 20 A/g.

Energy density (E) and power density (P), the two very significant parameters to evaluate the performance of supercapacitor devices, were calculated and displayed in the Ragone plot as depicted in Fig. 6a. Impressively, the $Cu(NiCo)_2S_4/Ni_3S_4$/AC HSC could deliver a high energy density of 40.8 Wh/kg at the power density of 785.5 W/kg and the maximum power density of 7859.2 W/kg at the energy density of 27.1 W/kg, which are preferable or comparable to most of supercapacitors based on cobalt/nickel/copper sulfides, oxides or hydroxides as shown in Fig. 6a and Table S1 in supporting information [31,44–48]. Long-term stability of energy storage device is quite significant for their practical applications. Therefore, the cycling performance of $Cu(NiCo)_2S_4/Ni_3S_4$/AC HSC was evaluated after 5000 cycles at the current density of 15 A/g. As shown in Fig. 5g, the assembled HSC exhibited outstanding long-term stability, where 85% of capacitive performance and 95.2% of coulombic efficiency were maintained after 5000 cycling tests. The GCD curves at the initial and final 10 cycles during the stability measurement are shown in the inset of Fig. 6b. The similar curves further verify the superior capacitive stability. Based on the favorable electrochemical performance of the assembled $Cu(NiCo)_2S_4/Ni_3S_4$/AC HSC, two of them were connected in series to explore their practical applications. Fig. 6c demonstrated that the series-wound two HSCs could light up a few red and yellow lighting-emitting diodes (LED) for several minutes. Besides, a fan motor could also be driven rotating with high speed, implying the promising application prospect of the fabricated $Cu(NiCo)_2S_4/Ni_3S_4$/AC HSC as a potential energy storage and conversion device.

4. Conclusions

In conclusion, we propose a novel and ingenious strategy to synthesize $Cu(NiCo)_2S_4/Ni_3S_4$ with 3D hierarchical hollow heterostructure utilizing Cu-Co biMOF as both the template and precursor. Compared with the traditional mono-metallic MOF, bimetal MOF shows quite versatile adjustability of structure. The sequent ion-exchange processes in the presence of Ni^{2+} and S^{2-} cannot only keep the morphology of initially obtained biMOF template but also generate hierarchical porous structures. As a result, the synthesized $Cu(NiCo)_2S_4/Ni_3S_4$ achieves superior specific capacitance, rate performance as well as cycle stability than those of CuNiCo-OH. The enhanced performance can be attributed to the synergetic effect resulted from the improved electronic conductivity, higher specific surface area and pore increase, which will enlarge the electrode and electrolyte contact area and shorten the path length for ion transport. Thus, this work has provided a reference method to design the multi-metal MOF derived trimetallic sulfides with 3D hollow structure for energy storage and conversion device.

CRediT authorship contribution statement

Wei Zhao: Conceptualization, Writing - original draft, Methodology. **Guowen Yan:** Writing - review & editing, Data curation. **Yiwei Zheng:** Visualization, Investigation. **Bingping Liu:** Formal analysis. **Dedong Jia:** Formal analysis. **Taiwei Liu:** Formal analysis. **Liang Cui:** Funding acquisition. **Rongkun Zheng:** Funding acquisition. **Di Wei:** Writing - review & editing. **Jingquan Liu:** Funding acquisition, Supervision.

Declaration of Competing Interest

The authors declare that they have no known competing financial interests or personal relationships that could have appeared to influence the work reported in this paper.

Acknowledgements

The authors acknowledge the National Natural Science Foundation of China (21805124) and Natural Science Foundation of Shandong Province (ZR2018BEM020). DW and RKZ acknowledge the Taishan Scholars Program. The authors also like to thank Shiyanjia Lab (www.shiyanjia.com) for support of XPS analysis.

Appendix A. Supplementary material

Supplementary data to this article can be found online at https://doi.org/10.1016/j.jcis.2020.01.049.

References

[1] R. Kotz, M. Carlen, Principles and applications of electrochemical capacitors, Electrochim. Acta. 45 (2000) 2483–2498.
[2] Y. Zheng, W. Zhao, D. Jia, L. Cui, J. Liu, Thermally-treated and acid-etched carbon fiber cloth based on pre-oxidized polyacrylonitrile as self-standing and high area-capacitance electrodes for flexible supercapacitors, Chem. Eng. J. 364 (2019) 70–78.
[3] F. Wang, X. Wu, X. Yuan, Z. Liu, Y. Zhang, L. Fu, Y. Zhu, Q. Zhou, Y. Wu, W. Huang, Latest advances in supercapacitors: from new electrode materials to novel device designs, Chem. Soc. Rev. 46 (2017) 6816–6854.
[4] Y. Yang, S. Li, W. Huang, H. Shangguan, C. Engelbrekt, S. Duan, L. Ci, P. Si, Effective synthetic strategy for $Zn_{0.76}Co_{0.24}S$ encapsulated in stabilized N-doped carbon nanoarchitecture towards ultra-long-life hybrid supercapacitors, J. Mater. Chem. A. 7 (2019) 14670–14680.
[5] M. Hu, C. Cui, C. Shi, Z.-S. Wu, J. Yang, R. Cheng, T. Guang, H. Wang, H. Lu, X. Wang, High-energy-density hydrogen-ion-rocking-chair hybrid supercapacitors based on $Ti_3C_2T_x$ MXene and carbon nanotubes mediated by redox active molecule, ACS Nano 13 (2019) 6899–6905.
[6] J. Li, Z. Liu, Q. Zhang, Y. Cheng, B. Zhao, S. Dai, H.-H. Wu, K. Zhang, D. Ding, Y. Wu, M. Liu, M.-S. Wang, Anion and cation substitution in transition-metal oxides nanosheets for high-performance hybrid supercapacitors, Nano Energy 57 (2019) 22–33.
[7] T. Wang, H.C. Chen, F. Yu, X.S. Zhao, H. Wang, Boosting the cycling stability of transition metal compounds-based supercapacitors, Energy Storage Mater. 16 (2019) 545–573.
[8] D.J. Vaughan, R.G. Burns, V.M. Burns, Geochemistry and bonding of thiospinel minerals, Cosmochim. Acta 35 (1971) 365–381.
[9] P. Geng, S. Zheng, H. Tang, R. Zhu, L. Zhang, S. Cao, H. Xue, H. Pang, Transition metal sulfides based on graphene for electrochemical energy storage, Adv. Energy Mater. 8 (2018) 1703259.
[10] A.M. Wiltrout, C.G. Read, E.M. Spencer, R.E. Schaak, Solution synthesis of thiospinel $CuCo_2S_4$ nanoparticles, Inorg. Chem. 55 (2016) 221–226.
[11] Y. Zhu, X. Chen, W. Zhou, K. Xiang, W. Hu, H. Chen, Controllable preparation of highly uniform $CuCo_2S_4$ materials as battery electrode for energy storage with enhanced electrochemical performances, Electrochim. Acta 249 (2017) 64–71.
[12] H. Li, Y. Sun, Z.-Y. Yuan, Y.-P. Zhu, T.-Y. Ma, Titanium phosphonate based metal-organic frameworks with hierarchical porosity for enhanced photocatalytic hydrogen evolution, Angew. Chem., Int. Ed. 57 (2018) 3222–3227.
[13] W. Liu, J. Huang, Q. Yang, S. Wang, X. Sun, W. Zhang, J. Liu, F. Huo, Multi-shelled hollow metal-organic frameworks, Angew. Chem., Int. Ed. 56 (2017) 5512–5516.
[14] S.-L. Hou, J. Dong, X.-L. Jiang, Z.-H. Jiao, B. Zhao, A noble-metal-free metal-organic framework (MOF) catalyst for the highly efficient conversion of CO_2 with propargylic alcohols, Angew. Chem., Int. Ed. 58 (2019) 577–581.
[15] Y. Wang, L. Feng, J. Pang, J. Li, N. Huang, G.S. Day, L. Cheng, H.F. Drake, Y. Wang, C. Lollar, J. Qin, Z. Gu, T. Lu, S. Yuan, H.-C. Zhou, Photosensitizer-anchored 2D MOF nanosheets as highly stable and accessible catalysts toward artemisinin production, Adv. Sci. 6 (2019) 1802059.
[16] B. Kim, J. Na, H. Lim, Y. Kim, J. Kim, E. Kim, Robust high thermoelectric harvesting under a self-humidifying bilayer of metal organic framework and hydrogel layer, Adv. Funct. Mater. 29 (2019) 1807549.
[17] S. Yuan, L. Zou, J.-S. Qin, J. Li, L. Huang, L. Feng, X. Wang, M. Bosch, A. Alsalme, T. Cagin, H.-C. Zhou, Construction of hierarchically porous metal-organic frameworks through linker labilization, Nat. Commun. 8 (2017) 15356.

[18] W. Lu, Z. Wei, Z.-Y. Gu, T.-F. Liu, J. Park, J. Park, J. Tian, M. Zhang, Q. Zhang, T. Gentle III, M. Bosch, H.-C. Zhou, Tuning the structure and function of metal-organic frameworks via linker design, Chem. Soc. Rev. 43 (2014) 5561–5593.
[19] Y. Wang, J. Huang, Y. Xiao, Z. Peng, K. Yuan, L. Tan, Y. Chen, Hierarchical nickel cobalt sulfide nanosheet on MOF-derived carbon nanowall arrays with remarkable supercapacitive performance, Carbon 147 (2019) 146–153.
[20] G. Zou, H. Hou, G. Zhao, P. Ge, D. Yin, X. Ji, N-rich carbon coated $CoSnO_3$ derived from in situ construction of a Co-MOF with enhanced sodium storage performance, J. Mater. Chem. A. 6 (2018) 4839–4847.
[21] J. Zhao, H. Li, C. Li, Q. Zhang, J. Sun, X. Wang, J. Guo, L. Xie, J. Xie, B. He, Z. Zhou, C. Lu, W. Lu, G. Zhu, Y. Yao, MOF for template-directed growth of well-oriented nanowire hybrid arrays on carbon nanotube fibers for wearable electronics integrated with triboelectric nanogenerators, Nano Energy 45 (2018) 420–431.
[22] T.G. Yun, M. Park, D.-H. Kim, D. Kim, J.Y. Cheong, J.G. Bae, S.M. Han, I.-D. Kim, All-transparent stretchable electrochromic supercapacitor wearable patch device, ACS Nano 13 (2019) 3141–3150.
[23] M. Liu, Z. Cong, X. Pu, W. Guo, T. Liu, M. Li, Y. Zhang, W. Hu, Z.L. Wang, High-energy asymmetric supercapacitor yarns for self-charging power textiles, Adv. Funct. Mater. 29 (2019) 1806298.
[24] G. Fang, J. Zhou, C. Liang, A. Pan, C. Zhang, Y. Tang, X. Tan, J. Liu, S. Liang, MOFs nanosheets derived porous metal oxide-coated three-dimensional substrates for lithium-ion battery applications, Nano Energy 26 (2016) 57–65.
[25] X. Deng, S. Zhu, J. Li, L. Ma, F. He, E. Liu, C. He, C. Shi, Q. Li, N. Zhao, Ball-in-cage nanocomposites of metal-organic frameworks and three-dimensional carbon networks: synthesis and capacitive performance, Nanoscale 9 (2017) 6478–6485.
[26] J. Liu, J. He, L. Wang, R. Li, P. Chen, X. Rao, L. Deng, L. Rong, J. Lei, NiO-PTA supported on ZIF-8 as a highly effective catalyst for hydrocracking of Jatropha oil, Sci. Rep. 6 (2016) 23667.
[27] C. Guan, X. Liu, W. Ren, X. Li, C. Cheng, J. Wang, Rational design of metal-organic framework derived hollow $NiCo_2O_4$ arrays for flexible supercapacitor and electrocatalysis, Adv. Energy Mater. 7 (2017) 1602391.
[28] Z. Xiao, L. Fan, B. Xu, S. Zhang, W. Kang, Z. Kang, H. Lin, X. Liu, S. Zhang, D. Sun, Green fabrication of ultrathin Co_3O_4 nanosheets from metal-organic framework for robust high-rate supercapacitors, ACS Appl. Mater. Interfaces 9 (2017) 41827–41836.
[29] L. Qian, L. Gu, L. Yang, H. Yuan, D. Xiao, Direct growth of $NiCo_2O_4$ nanostructures on conductive substrates with enhanced electrocatalytic activity and stability for methanol oxidation, Nanoscale 5 (2013) 7388–7396.
[30] J.-J. Duan, X.-X. Zheng, H.-J. Niu, J.-J. Feng, Q.-L. Zhang, H. Huang, A.-J. Wang, Porous dendritic PtRuPd nanospheres with enhanced catalytic activity and durability for ethylene glycol oxidation and oxygen reduction reactions, J. Colloid Interface Sci. 560 (2020) 467–474.
[31] G. Nagaraju, S.C. Sekhar, J.S. Yu, Utilizing waste cable wires for high-performance fiber-based hybrid supercapacitors: an effective approach to electronic-waste management, Adv. Energy Mater. 8 (2018) 1702201.
[32] P. Yang, Z. Wu, Y. Jiang, Z. Pan, W. Tian, L. Jiang, L. Hu, Fractal $(Ni_xCo_{1-x})_9Se_8$ nanodendrite arrays with highly exposed $(01\bar{1})$ surface for wearable, all-solid-state supercapacitor, Adv. Energy Mater. 8 (2018) 1801392.
[33] Y. Chen, X.-X. Zheng, X.-Y. Huang, A.-J. Wang, Q.-L. Zhang, H. Huang, J.-J. Feng, Trimetallic PtRhCo petal-assembled alloyed nanoflowers as efficient and stable bifunctional electrocatalyst for ethylene glycol oxidation and hydrogen evolution reactions, J. Colloid Interface Sci. 559 (2020) 206–214.
[34] H.-J. Niu, L. Zhang, J.-J. Feng, Q.-L. Zhang, H. Huan, A.-J. Wang, Graphene-encapsulated cobalt nanoparticles embedded in porous nitrogen-doped graphitic carbon nanosheets as efficient electrocatalysts for oxygen reduction reaction, J. Colloid Interface Sci. 552 (2019) 744–751.
[35] W. Zhao, Y. Zheng, L. Cui, D. Jia, D. Wei, R. Zheng, C. Barrow, W. Yang, J. Liu, MOF derived Ni-Co-S nanosheets on electrochemically activated carbon cloth via an etching/ion exchange method for wearable hybrid supercapacitors, Chem. Eng. J. 371 (2019) 461–469.
[36] F.B. Ajdari, E. Kowsari, A. Ehsani, M. Schorowski, T. Ameri, New synthesized ionic liquid functionalized graphene oxide: Synthesis, characterization and its nanocomposite with conjugated polymer as effective electrode materials in an energy storage device, Electrochim. Acta 292 (2018) 789–804.
[37] E. Kowsari, A. Ehsani, M.D. Najafi, N. Seifvand, A.A. Heidari, Geminal dicationic ionic liquid functionalized graphene nanoribbon/POAP composite film: synthesis, characterization and electrochemical pseudocapacitance performance, Ionics 24 (2018) 2083–2092.
[38] E. Kowsari, A. Ehsani, M.D. Najafi, M. Bigdeloo, Enhancement of pseudocapacitance performance of p-type conductive polymer in the presence of newly synthesized graphene oxide-hexamethylene tributylammonium iodide nanosheets, J. Colloid Interface Sci. 512 (2018) 346–352.
[39] E. Kowsari, A. Ehsani, M.D. Najafi, Electrosynthesis and pseudocapacitance performance of ionic liquid-$Cr(\eta^6\text{-}C_6H_5)$ complex functionalized reduced graphene oxide/poly ortho aminophenol nanocomposite film, J. Colloid Interface Sci. 504 (2017) 507–513.
[40] F.B. Ajdari, E. Kowsari, A. Ehsani, Ternary nanocomposites of conductive polymer/functionalized GO/MOFs: synthesis, characterization and electrochemical performance as effective electrode materials in pseudocapacitors, J. Solid State Chem. 265 (2018) 155–166.
[41] G. Zhang, X.W. Lou, General solution growth of mesoporous $NiCo_2O_4$ nanosheets on various conductive substrates as high-performance electrodes for supercapacitors, Adv. Mater. 25 (2013) 976–979.
[42] Y. Huang, M. Zhong, Y. Huang, M. Zhu, Z. Pei, Z. Wang, Q. Xue, X. Xie, C. Zhi, A self-healable and highly stretchable supercapacitor based on a dual crosslinked polyelectrolyte, Nat. Commun. 6 (2015) 10310.
[43] X. Xu, Y. Liu, P. Dong, P.M. Ajayan, J. Shen, M. Ye, Mesostructured $CuCo_2S_4$/$CuCo_2O_4$ nanoflowers as advanced electrodes for asymmetric supercapacitors, J. Power Sources. 400 (2018) 96–103.
[44] Y. Wang, S. Nie, Y. Liu, W. Yan, S. Lin, G. Cheng, H. Yang, J. Luo, Room-temperature fabrication of a nickel-functionalized copper metal-organic framework (Ni@Cu-MOF) as a new pseudocapacitive material for asymmetric supercapacitors, Polymers 11 (2019) 821.
[45] Z. Xiao, Y. Mei, S. Yuan, H. Mei, B. Xu, Y. Bao, L. Fan, W. Kang, F. Dai, R. Wang, L. Wang, S. Hu, D. Sun, H.-C. Zhou, Controlled hydrolysis of metal-organic frameworks: hierarchical Ni/Co-layered double hydroxide microspheres for high-performance supercapacitors, ACS Nano 13 (2019) 7024–7030.
[46] S.G. Mohamed, I. Hussain, J.-J. Shim, One-step synthesis of hollow C-$NiCo_2S_4$ nanostructures for high-performance supercapacitor electrodes, Nanoscale 10 (2018) 6620–6628.
[47] Y. Liu, G. Liu, X. Nie, A. Pan, S. Liang, T. Zhu, In situ formation of Ni3S2-Cu1.8S nanosheets to promote hybrid supercapacitor performance, J. Mater. Chem. A. 7 (2019) 11044–11052.
[48] Y. Zheng, X. Wang, W. Zhao, X. Cao, J. Liu, Phytic acid-assisted synthesis of ultrafine $NiCo_2S_4$ nanoparticles immobilized on reduced graphene oxide as high-performance electrode for hybrid supercapacitors, Chem. Eng. J. 333 (2018) 603–612.